

Spectroscopy and Thermometry of Drumhead Modes in a Mesoscopic Trapped-Ion Crystal using Entanglement

Brian C. Sawyer,^{1,*} Joseph W. Britton,¹ Adam C. Keith,^{2,†} C.-C. Joseph Wang,²
James K. Freericks,² Hermann Uys,³ Michael J. Biercuk,⁴ and John J. Bollinger¹

¹*Time and Frequency Division, National Institute of Standards and Technology, Boulder, CO 80305*

²*Department of Physics, Georgetown University, Washington, DC 20057*

³*Council for Scientific and Industrial Research, Pretoria, South Africa*

⁴*Centre for Engineering Quantum Systems, School of Physics, The University of Sydney, NSW Australia*

We demonstrate spectroscopy and thermometry of individual motional modes in a mesoscopic 2D ion array using entanglement-induced decoherence as a method of transduction. Our system is a $\sim 400 \mu\text{m}$ -diameter planar crystal of several hundred ${}^9\text{Be}^+$ ions exhibiting complex drumhead modes in the confining potential of a Penning trap. Exploiting precise control over the ${}^9\text{Be}^+$ valence electron spins, we apply a homogeneous spin-dependent optical dipole force to excite arbitrary transverse modes with an effective wavelength approaching the interparticle spacing ($\sim 20 \mu\text{m}$). Center-of-mass displacements below 1 nm are detected via entanglement of spin and motional degrees of freedom.

PACS numbers: 52.27.Jt, 52.27.Aj, 03.65.Ud, 03.67.Bg

Studies of quantum physics at the interface of microscopic and mesoscopic regimes have recently focused on the observation of quantum coherent phenomena in optomechanical systems [1–3]. The realization of quantum coherence in mechanical oscillations involving many particles behaving approximately as a continuum provides exciting insights into the quantum-classical transition. Previous work has shown that crystals of cold, trapped ions behave as atomic-scale nanomechanical oscillators [4–6], with the benefits of in-situ tunable motional modes and exploitable single-particle quantum degrees of freedom (e.g. valence electron spin). Our system of hundreds of crystallized ions in a Penning trap provides a bottom-up approach to studying mesoscopic quantum coherence. In this context, the relevant particle numbers are sufficiently small to permit excellent quantum control without sacrificing continuum mechanical features. Beyond these capabilities, trapped ions have long provided a laboratory platform for studying diverse physical phenomena including: strongly-coupled one-component plasmas (OCPs) [7, 8]; quantum computation [9, 10] and simulation [11–15]; dynamical decoupling [16]; and atomic clocks and precision measurement [17].

In this Letter, we present an experimental and theoretical study of motional drumhead modes in a 2D crystal of ${}^9\text{Be}^+$ ions confined within a Penning trap. We excite *inhomogeneous* modes of arbitrary wavelength (see Fig. 1(a)) through application of a *homogeneous*, spin-state-dependent optical dipole force (ODF) to a large-scale spin superposition. Distinct drumhead modes are entangled with the ${}^9\text{Be}^+$ valence electron spins by tuning a beat frequency (μ_R) between two ODF lasers near a mode resonance. This spin-motion entanglement is de-

tected as a μ_R -dependent decoherence of ion spins whose magnitude conveys the specific mode temperature.

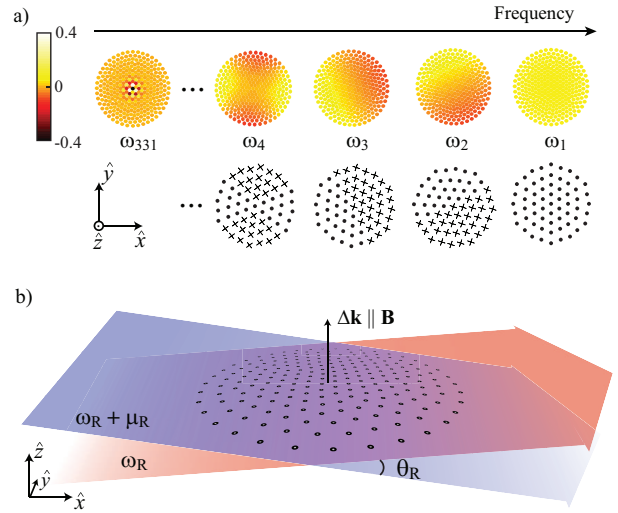


FIG. 1: (color online) (a) Calculated structure of selected transverse eigenmodes (\vec{b}_m) for a 2D crystal of 331 ${}^9\text{Be}^+$ ions. Mode frequencies, ω_m , decrease as effective wavelength gets shorter. The arbitrary color scale indicates relative ion displacement amplitude. One example of an ion spin state with similar symmetry is given below each of the four highest-frequency eigenmodes. The symbol \times (\bullet) denotes spin-projection into (out of) the plane. Interaction between these spin and mode configurations mediated by the spin-dependent optical dipole force (ODF) leads to excitation of the corresponding eigenmode. (b) Illustration of a single plane of ${}^9\text{Be}^+$ within the Penning trap. Two 313-nm beams intersect at the ion cloud to form a traveling wave of beat frequency μ_R and effective wavevector $\vec{\Delta k}$ along the direction of the trap magnetic field. The electric field intensity is uniform in the plane, but the spin-dependent induced AC Stark shift permits excitation of transverse modes of arbitrary wavelength.

*Electronic address: brian.sawyer@boulder.nist.gov

†Department of Physics, North Carolina State University, Raleigh, NC 27695

Previous global mode studies on 2D planar ion arrays were restricted to modes with wavelengths on the order of the cloud size [18–22]. By contrast, the short-wavelength modes studied here are of particular interest due to their increased sensitivity to strong-correlation corrections [23, 24] compared to those with long wavelength, which are well-described by fluid theory. Thermometry of large Coulomb crystals has thus far been limited to determination of global temperature through Doppler profile measurements [25], which give a minimum sensitivity of ~ 0.5 mK in ${}^9\text{Be}^+$. Our temperature measurement is mode-specific and may be employed below the Doppler cooling limit, providing an alternative to Raman sideband thermometry [26].

The Penning trap used for this work is detailed in a previous publication [27]. Application of static voltages to a stack of cylindrical electrodes provides harmonic confinement along \hat{z} (the trap symmetry axis) with a ${}^9\text{Be}^+$ center-of-mass (COM) oscillation frequency of $\omega_1/2\pi = 795$ kHz that is independent of the number of trapped ions. The trap resides within the room-temperature bore of a superconducting magnet, and radial confinement is achieved via the Lorentz force generated by rotation of the ion cloud through the static, homogeneous magnetic (B) field of ~ 4.46 T oriented along \hat{z} . Application of a time-dependent quadrupole ‘rotating wall’ potential permits phase-stable control of the rotation frequency (ω_r), and thus the confining radial force of the trap [28, 29]. In the limit of a weak rotating wall potential, the harmonic trap potential in a frame rotating at ω_r is [8]

$$q\Phi_{\text{trap}}(r, z) = \frac{1}{2}M\omega_1^2(z^2 + \beta r^2), \quad (1)$$

$$\beta = \frac{\omega_r(\Omega_c - \omega_r)}{\omega_1^2} - \frac{1}{2} \quad (2)$$

where M (q) is the mass (charge) of a single ${}^9\text{Be}^+$, $\Omega_c = 2\pi \times 7.6$ MHz is the cyclotron frequency, and z (r) is axial (radial) distance from the trap center. We set the rotation frequency, ω_r , such that the radial confinement is weak relative to transverse confinement ($\beta \ll 1$), resulting in a single ion plane.

The $m_J = \pm 1/2$ projections of the $\text{Be}^+ {}^2S_{1/2}$ ground state are split by ~ 124 GHz and serve as $|\uparrow\rangle$ and $|\downarrow\rangle$ ‘qubit’ states, respectively. Global spin rotations are performed by injecting 124-GHz radiation through a waveguide attached to the side of the trap. The ${}^9\text{Be}^+$ ions are Doppler laser cooled with laser beams directed both parallel and perpendicular to \hat{z} . Both beams are tuned to the ${}^2S_{1/2}(m_J = +1/2) \rightarrow {}^2P_{3/2}(m_J = +3/2)$ transition at ~ 313 nm to cool ion motion below 1 mK. This same transition is used for ion detection and projective spin-state measurement. Discrimination of $|\uparrow\rangle$ (bright) from $|\downarrow\rangle$ (dark) is performed with a fidelity $> 99\%$ [27].

The axial and radial confining potentials are tuned to yield a planar ion configuration. Due to mutual Coulomb repulsion and the low ion temperature, the ions’

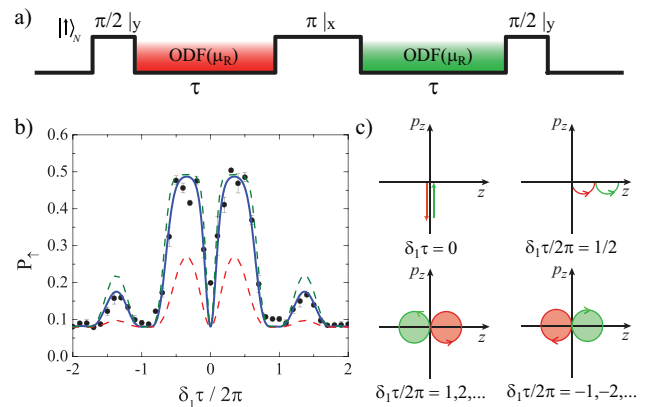


FIG. 2: (color online) (a) Pulse sequence used for excitation and detection of transverse motional modes. Global spin rotations are performed with microwaves at ~ 124 GHz, while the state-dependent optical dipole force is applied in each arm of the spin echo for a duration τ . We implement π -pulse times (t_π) as short as $65 \mu\text{s}$. (b) Measured (points with statistical error bars) and fit (solid blue line) probability of detecting $|\uparrow\rangle$ (P_\uparrow) at the end of the spin echo sequence. Frequency-dependent decoherence is due to entanglement of spins with the axial COM mode ($\omega_1/2\pi = 795$ kHz) as a function of ODF detuning $\delta_1 \equiv \mu_R - \omega_1$ in a cloud of 190 ± 8 ions. Each point is an average of 90 experimental runs. The fit provides a mode temperature of 2.3 ± 0.5 mK, whose error includes a 5% uncertainty in ODF beam angle, θ_R . For comparison, the lower (upper) dashed line is calculated assuming 0.4 mK (4.0 mK). (c) Illustrated phase-space trajectories of state $|\uparrow\rangle_N$ at different detunings, δ_1 , in a frame rotating at ω_1 . Axis labels represent center-of-mass momentum ($p_z \propto \text{Im}[\alpha_{j1}]$) and position ($z \propto \text{Re}[\alpha_{j1}]$).

minimum-energy configuration is a 2D crystal with triangular order [30]. Ion spacing is $\sim 20 \mu\text{m}$, and individual ions can be resolved using stroboscopic imaging at ω_r . The planar array of N ions exhibits $3N$ motional modes, N of which are drumhead oscillations transverse to the crystal plane (see Fig. 1(a)). As with 1D ion strings, the frequencies of these transverse modes decrease with decreasing effective wavelength due to screening of confining electric fields by nearby ions. The transverse eigenvectors (\vec{b}_m , $m \in [1, N]$) and corresponding eigenfrequencies (ω_m) are obtained by first numerically calculating the zero-temperature 2D ion configuration in the presence of the Penning trap potentials. Applying a Taylor expansion of the combined trap and Coulomb potential about each ion equilibrium position, we diagonalize the $N \times N$ stiffness matrix whose eigenvalues and unit eigenvectors are ω_m and \vec{b}_m , respectively [31, 32]. The relative displacement amplitude of an ion j is given by the j th element of \vec{b}_m , denoted as b_{jm} , where $\sum_m |b_{jm}|^2 = \sum_j |b_{jm}|^2 = 1$.

To excite transverse modes in our 2D Coulomb crystal, we employ a spin-dependent ODF generated by interfering two off-resonant laser beams at the ion cloud position. This is depicted schematically in Fig. 1(b). The

two ODF beams are produced from a single beam using a 50/50 beamsplitter and subsequently pass through separate acousto-optic modulators that allow fast ($\sim 1 \mu\text{s}$) switching and impart a relative detuning μ_R . The beams intersect at an angle of $\theta_R = 4.8^\circ \pm 0.2^\circ$ at the ion cloud position, and their relative alignment is adjusted to orient the effective wavevector ($\Delta\vec{k}$) of the resulting standing ($\mu_R = 0$) or traveling ($\mu_R \neq 0$) wave to within $\sim 0.05^\circ$ of \hat{z} . The common wavelength (313.133 nm) and unique linear polarizations of the beams are chosen such that the AC Stark shift from the interfering beams on state $|\uparrow\rangle$ is equal in magnitude and opposite in sign to that on $|\downarrow\rangle$ [33]. The result of the interference between these two beams is a spin-dependent force on each ion, j ($F_{\uparrow,j} = -F_{\downarrow,j} \equiv F_j$). The Hamiltonian for this interaction is $\hat{H}_{\text{ODF}} = -\sum_{j=1}^N F_j \hat{z}_j(t) \cos(\mu_R t) \hat{\sigma}_j^z$, where $\hat{z}_j(t)$ is the time-dependent position operator and $\hat{\sigma}_j^z$ is the z -component Pauli operator for ion j [14]. The elliptical beam waists ($100 \mu\text{m} \times 1000 \mu\text{m}$, with the major axis oriented parallel to the ion plane [33]) are sufficiently large to generate an approximately uniform ODF with variation below 10% across the $\sim 400 \mu\text{m}$ -diameter planar ion crystal. Typical ODFs for this work are $F_j \sim 10^{-23} \text{ N}$ along \hat{z} .

Figure 2(a) illustrates the experimental control sequence for microwaves (black line) and ODF lasers (shaded regions) used to coherently excite transverse modes of motion. Ions are first prepared in the ‘bright’ state $|\uparrow\rangle_N \equiv \prod_{j=1}^N |\uparrow_j\rangle$ via optical pumping [27]. The sequence of microwave pulses in Fig. 2(a) comprises a spin echo (SE) [34] that, in the absence of the ODF beams, rotates the ions to the ‘dark’ state $|\downarrow\rangle_N$ with $>99\%$ fidelity. The SE cancels low-frequency precession about \hat{z} due to ODF laser intensity and magnetic field fluctuations as well as microwave phase noise [16, 35]. The spin-dependent ODF is applied in each arm of the SE for a duration τ .

The initial microwave pulse rotates each spin by $\pi/2$ to produce the state $\prod_{j=1}^N \frac{1}{\sqrt{2}} (|\uparrow_j\rangle - |\downarrow_j\rangle)$, which is a superposition of all possible (2^N) spin permutations. Importantly, it is the creation of this state that permits subsequent excitation of arbitrary transverse modes with our homogeneous, spin-dependent ODF. By tuning μ_R near a mode of frequency ω_m , the spin-dependent ODF excites those components of the spin superposition with approximately the same symmetry as the eigenvector \vec{b}_m . A subset of these eigenvectors and associated spin states are illustrated in Fig. 1(a). Depending on experimental parameters, the spin states may be entangled with different motional states at the end of the control sequence of Fig. 2(a). Upon measurement of the spin state (performing a trace over the motion), entanglement is manifested as spin decoherence that varies with μ_R . We observe this as a decrease in the length of the spins’ Bloch vector and a concomitant increase in the probability (P_\uparrow) of measuring state $|\uparrow\rangle$ averaged over all ions.

Figure 2(b) gives experimental and theoretical results for a sweep of μ_R near the COM frequency, ω_1 , with $\tau = 500 \mu\text{s}$ and $\delta_1 = (\mu_R - \omega_1)$. On resonance ($\delta_1 = 0$), the pulse sequence leads to excitation (de-excitation) of the COM mode in the first (second) arm. When the product $|\delta_1 \tau / 2\pi| = l$ is a non-zero integer, each spin state traverses l full loops in phase space over τ (see Fig. 2(c)). At intermediate detunings, the spin and motion remain entangled at the end of the pulse sequence, producing the lineshape of Fig. 2(b). These motional excitations are described by the spin-dependent displacement operator $\hat{U}(\tau) = \prod_{j,m} \exp[(\alpha_{jm} \hat{a}_m^\dagger - \alpha_{jm}^* \hat{a}_m) \hat{\sigma}_j^z]$ [32, 33, 36], where $\alpha_{jm}(\tau)$ is the coherently-driven complex displacement amplitude for ion j of mode m , and \hat{a}_m^\dagger (\hat{a}_m) is the creation (annihilation) operator for mode m . Accounting for both arms of the pulse sequence, we obtain [33]

$$\alpha_{jm} = \frac{F_j b_{jm}}{\hbar(\mu_R^2 - \omega_m^2)} \sqrt{\frac{\hbar}{2M\omega_m}} [\omega_m(1 - \cos\phi) + i\mu_R \sin\phi - e^{i\omega_m\tau} \{\omega_m [\cos(\mu_R\tau) - \cos(\mu_R\tau + \phi)] - i\mu_R [\sin(\mu_R\tau) - \sin(\mu_R\tau + \phi)]\}], \quad (3)$$

where \hbar is Planck’s constant, F_j is the ODF magnitude on ion j , and $\phi = (\tau + t_\pi)(\mu_R - \omega_m)$ accounts for phase evolution of the ODF drive relative to that of the mode.

Although the coherently driven, spin-dependent displacements (α_{jm}) are independent of the initial motional state (assuming Lamb-Dicke confinement [14]), the spin-motion entanglement signal in Fig. 2(b) sensitively depends on this initial state. This can be qualitatively understood in terms of the spatial structure of a harmonic oscillator Fock state, $|n_m\rangle$, of mode m . A state $|n_m\rangle$ exhibits n wavefunction nodes and therefore, as n increases, a fixed spin-dependent displacement results in less wavefunction overlap between different spin components due

to the increasing spatial frequency of $|n_m\rangle$ wavefunctions. This leads to larger decoherence and greater displacement sensitivity as the average mode occupation, \bar{n}_m , is increased for a given mode. We fit the experimental measurements in Fig. 2(b) using theory that attributes a thermal state of motion to each mode m characterized by mode occupation $\bar{n}_m \sim k_B T_m (\hbar\omega_m)^{-1}$ and temperature T_m . Neglecting spin-spin correlation contributions, we find the probability $P_\uparrow^{(j)}$ of detecting ion j in state $|\uparrow\rangle$ at the end of the pulse sequence to be [33]

$$P_\uparrow^{(j)} = \frac{1}{2} \left[1 - e^{-2\Gamma\tau} \exp\left(-2 \sum_m |\alpha_{jm}|^2 (2\bar{n}_m + 1)\right) \right]. \quad (4)$$

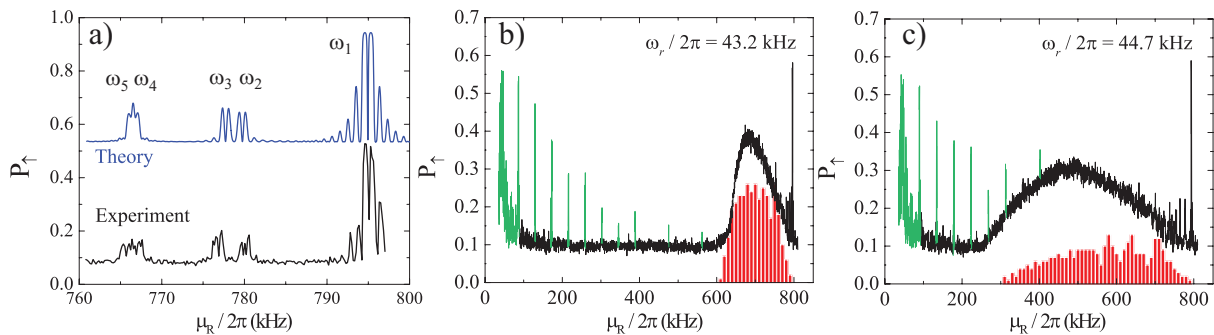


FIG. 3: (color online) (a) Measured (lower) and calculated (offset) probabilities for measuring $|\uparrow\rangle$ after the spin echo sequence as a function of ODF beat frequency for a sweep of μ_R over the first five transverse modes with 250 ± 15 ions. The modes at ω_2 and ω_3 are split due to distortion of the ion cloud boundary by the rotating wall potential. Panels (b) and (c) give results of wider sweeps with $\omega_r/2\pi = 43.2$ kHz and 44.7 kHz, respectively, in a crystal of 345 ± 25 ions. Frequency-dependent deviation from $P_\uparrow \sim 0.1$ is due to spin-motional entanglement, while the background is due to spontaneous emission from the ODF beams. The histogram (red bars) shown below each experimental curve depicts the density of calculated eigenmodes at the given ω_r . Histogram bins are 10 kHz wide and plotted with an arbitrary vertical scale. As described in Fig. 1(a), the highest-frequency feature is that of the COM mode and the ~ 50 lowest-frequency eigenmodes include nearest-neighbor ions oscillating out of phase. Features at ω_r and precise harmonics thereof (shaded in light green) are due to spin-motion entanglement with in-plane degrees of freedom excited by the small ($\sim 10^{-3} F_j$) component of ODF perpendicular to \hat{z} .

Here Γ accounts for decoherence due to spontaneous emission induced by the ODF lasers over the duration 2τ , and is responsible for the background level of $P_\uparrow \sim 0.1$ observed in all experimental data presented here [37]. The total detection probability P_\uparrow is obtained by averaging all $P_\uparrow^{(j)}$.

For interaction with the COM mode ($b_{j1} = \frac{1}{\sqrt{N}}, \forall j \in [1, N]$), α_{j1} is obtained from Eq. (3) through measurement of the ODF laser intensities [14] and trapped-ion number, while Γ is determined from decoherence observed with μ_R detuned far from any modes. As such, the only parameter of Eq. (4) not measured directly is \bar{n}_1 , which is varied to fit experimental data as in Fig. 2(b), where we obtain $\bar{n}_1 = 60 \pm 13$ ($T_1 = 2.3 \pm 0.5$ mK).

We note that a detectable phase-space displacement is obtained with a very small amplitude of $|\alpha_{jm}|$. For example, in Fig. 2(b), the 20% decrease in the Bloch vector at $\delta_1\tau/2\pi \simeq \pm 1.4$ corresponds to a spin-state-dependent excitation of the COM mode with a mean excursion of ~ 0.6 nm in each arm of the pulse sequence. This shift is less than 0.2% of the wavefunction spread of a single ion in the planar array. Our sensitivity to displacements improves with increasing mode temperature provided that the ODF is adjusted to avoid full decoherence ($P_\uparrow = 0.5$) at the detuning of interest.

Figure 3(a) shows the result of a sweep of μ_R over five transverse modes and corresponding theory. The theoretical spectrum (offset for clarity) is generated assuming $T_1 = 10$ mK and $T_{m>1} = 0.4$ mK, with T_1 obtained from a fit. The large COM temperature of Fig. 3(a) is produced by quickly switching off the \hat{z} -oriented Doppler cooling beam on a time scale of $\sim 2\pi\omega_1^{-1}$. In this case, sudden loss of radiation pressure from the cooling light induces a COM oscillation amplitude of ~ 50 nm that we detect as an elevated \bar{n}_1 . A more adiabatic reduction of

the cooling beam intensity yields $\bar{n}_1 \sim 26$ ($T_1 \sim 1$ mK). For modes other than the COM, we must additionally calculate the b_{jm} values for the trap potentials and ion number in a given experiment. For these modes, we find temperatures consistent with the Doppler cooling limit of 0.43 mK.

To measure the full spectrum of transverse modes, we repeat the sequence of Fig. 2(a) for $30 \text{ kHz} \leq \mu_R/2\pi \leq 800 \text{ kHz}$ with $\tau = 1$ ms. With the exception of the COM mode, the frequencies of the remaining $N - 1$ modes depend sensitively on our choice of crystal rotation frequency, ω_r [20]. Figures 3(b)-(c) show the result of these experimental runs for $\omega_r/2\pi = 43.2$ kHz and 44.7 kHz, respectively. For this ion number of 345 ± 25 , the single-plane configuration is stable over the range $42.2 \text{ kHz} \lesssim \omega_r/2\pi \lesssim 45.2 \text{ kHz}$. Histograms of calculated mode density versus $\mu_R/2\pi$ are plotted below each experimental curve with an arbitrary vertical scale and bin width of 10 kHz. The distribution of eigenfrequencies narrows as ω_r is decreased; weaker radial confinement (see Eq. (2)) leads to lower ion densities and reduced screening of trap potentials, thereby moving the frequency of the shortest-wavelength mode toward that of the COM. This behavior is clearly visible in Figs. 3(b)-(c). Additionally, we find quantitative agreement between the measured spectrum and that generated from numerical calculation of the transverse eigenmodes under the given experimental conditions, documenting coupling to both short- and long-wavelength modes. The sharp features of Figs. 3(b)-(c) shaded in light green reflect excitation of in-plane resonances at harmonics of ω_r due to a very small component of the ODF ($\sim 10^{-3} F_j$) along the ion plane. These spectral features may be reduced through more careful alignment of $\vec{\Delta k}$ to \hat{z} , but their strong response suggests an elevated motional tempera-

ture perpendicular to \hat{z} .

In summary, we have used entanglement of spin and motional degrees of freedom to map the full transverse mode spectrum of a mesoscopic 2D ion array. This technique provides a tool for sensitively and accurately measuring the temperature and displacement amplitude of individual drumhead modes, facilitating identification of mode-specific heating mechanisms and the resulting non-equilibrium energy distributions. Coherent, spin-dependent excitation of transverse modes is the basis for engineering quantum spin-spin interactions with trapped ions [11–14, 31, 32, 38, 39], making mode characterization a critical element of such experiments. Future work will include investigation of low-frequency in-plane modes at frequencies smaller than ω_r . A predicted subset of these

modes includes in-plane shearing motion whose restoring force is due exclusively to strong correlations.

This work was supported by the DARPA-OLE program and NIST. B. C. Sawyer is supported by a NRC fellowship funded by NIST. M. J. Biercuk and J. J. Bollinger acknowledge partial support from the ARC Centre of Excellence for Engineered Quantum Systems, CE110001013. A. C. Keith was supported by the NSF under grant number DMR-1004268. J. K. Freericks was supported by the McDevitt endowment bequest at Georgetown University. We thank D.H.E. Dubin, D. Porras, K.-K. Ni, D. Slichter, and S. Manmana for comments on the manuscript. This manuscript is a contribution of NIST and not subject to U.S. copyright.

-
- [1] A. D. O’Connell et al., *Nature* **464**, 697 (2010).
 - [2] T. J. Kippenberg and K. J. Vahala, *Science* **321**, 1172 (2008).
 - [3] J. D. Teufel, T. Donner, M. A. Castellanos-Beltran, J. W. Harlow, and K. W. Lehnert, *Nat. Nanotechnol.* **4**, 820 (2009).
 - [4] M. J. Biercuk, J. W. Britton, H. Uys, A. VanDevender, and J. J. Bollinger, *Nat. Nanotechnol.* **5**, 646 (2010).
 - [5] J. D. Jost, J. P. Home, J. M. Amini, D. Hanneke, R. Ozeri, C. Langer, J. J. Bollinger, D. Leibfried, and D. J. Wineland, *Nature* **459**, 683 (2009).
 - [6] K. R. Brown, C. Ospelkaus, Y. Colombe, A. C. Wilson, and D. J. Wineland, *Nature* **471**, 196 (2011).
 - [7] S. Ichimaru, *Rev. Mod. Phys.* **54**, 1017 (1982).
 - [8] D. H. E. Dubin and T. M. O’Neil, *Rev. Mod. Phys.* **71**, 87 (1999).
 - [9] D. Hanneke, J. P. Home, J. M. Amini, D. Leibfried, and D. J. Wineland, *Nature Phys.* **6**, 13 (2009).
 - [10] T. Monz et al., *Phys. Rev. Lett.* **103**, 200503 (2009).
 - [11] A. Friedenauer, H. Schmitz, J. T. Glueckert, D. Porras, and T. Schaetz, *Nature Phys.* **4**, 757 (2008).
 - [12] K. Kim, M.-S. Chang, S. Korenblit, R. Islam, E. E. Edwards, J. K. Freericks, G.-D. Lin, L.-M. Duan, and C. Monroe, *Nature* **465**, 590 (2010).
 - [13] R. Islam et al., *Nat. Commun.* **2**, 377 (2011).
 - [14] J. W. Britton et al., *Nature* **484**, 489 (2012).
 - [15] B. P. Lanyon et al., *Science* **334**, 57 (2011).
 - [16] M. J. Biercuk, H. Uys, A. P. VanDevender, N. Shiga, W. M. Itano, and J. J. Bollinger, *Nature* **458**, 996 (2009).
 - [17] T. Rosenband et al., *Science* **319**, 1808 (2008).
 - [18] D. J. Heinzen, J. J. Bollinger, F. L. Moore, W. M. Itano, and D. J. Wineland, *Phys. Rev. Lett.* **66**, 2080 (1991).
 - [19] J. J. Bollinger, D. J. Heinzen, F. L. Moore, W. M. Itano, D. J. Wineland, and D. H. E. Dubin, *Phys. Rev. A* **48**, 525 (1993).
 - [20] C. S. Weimer, J. J. Bollinger, F. L. Moore, and D. J. Wineland, *Phys. Rev. A* **49**, 3842 (1994).
 - [21] M. D. Tinkle, R. G. Greaves, C. M. Surko, R. L. Spencer, and G. W. Mason, *Phys. Rev. Lett.* **72**, 352 (1994).
 - [22] A. Dantan, J. P. Marler, M. Albert, D. Guénot, and M. Drewsen, *Phys. Rev. Lett.* **105**, 103001 (2010).
 - [23] J. M. Kriesel, J. J. Bollinger, T. B. Mitchell, L. B. King, and D. H. E. Dubin, *Phys. Rev. Lett.* **88**, 125003 (2002).
 - [24] J. Castro, P. McQuillen, and T. C. Killian, *Phys. Rev. Lett.* **105**, 065004 (2010).
 - [25] M. J. Jensen, T. Hasegawa, and J. J. Bollinger, *Phys. Rev. A* **70**, 033401 (2004).
 - [26] C. Monroe et al., *Phys. Rev. Lett.* **75**, 4011 (1995).
 - [27] M. J. Biercuk, H. Uys, A. P. VanDevender, N. Shiga, W. M. Itano, and J. J. Bollinger, *Quantum Info. and Comp.* **9**, 920 (2009).
 - [28] T. Hasegawa, M. J. Jensen, and J. J. Bollinger, *Phys. Rev. A* **71**, 023406 (2005).
 - [29] X.-P. Huang, J. J. Bollinger, T. B. Mitchell, W. M. Itano, and D. H. E. Dubin, *Phys. Plasmas* **5**, 1656 (1998).
 - [30] T. B. Mitchell, J. J. Bollinger, D. H. E. Dubin, X.-P. Huang, W. M. Itano, and R. H. Baughman, *Science* **282**, 1290 (1998).
 - [31] S.-L. Zhu, C. Monroe, and L.-M. Duan, *Phys. Rev. Lett.* **97**, 050505 (2006).
 - [32] K. Kim, M.-S. Chang, R. Islam, S. Korenblit, L.-M. Duan, and C. Monroe, *Phys. Rev. Lett.* **103**, 120502 (2009).
 - [33] See Supplemental Material for technical details and derivations.
 - [34] E. L. Hahn, *Phys. Rev.* **80**, 580 (1950).
 - [35] H. Uys, M. J. Biercuk, and J. J. Bollinger, *Phys. Rev. Lett.* **103**, 040501 (2009).
 - [36] C. Monroe, D. M. Meekhoff, B. E. King, and D. J. Wineland, *Science* **272**, 1131 (1996).
 - [37] H. Uys, M. J. Biercuk, A. VanDevender, C. Ospelkaus, D. Meiser, R. Ozeri, and J. J. Bollinger, *Phys. Rev. Lett.* **105**, 200401 (2010).
 - [38] D. Porras and J. I. Cirac, *Phys. Rev. Lett.* **92**, 207901 (2004).
 - [39] D. Porras and J. I. Cirac, *Phys. Rev. Lett.* **96**, 250501 (2006).

Supplementary Material:
Spectroscopy and Thermometry of Drumhead Modes in a Mesoscopic Trapped-Ion Crystal using Entanglement

Optical Dipole Force Details

Figure 4 shows a simple sketch of the optical dipole force (ODF) laser beam set-up. As discussed below, the frequency as well as the beam polarizations were chosen to null the AC Stark shift from an individual beam and to produce a state-dependent force which is equal in magnitude but opposite in sign for the $|\uparrow\rangle$ and $|\downarrow\rangle$ qubit states ($F_\uparrow = -F_\downarrow$). The off-resonant laser beam frequency was detuned from the cycling transition ($|\uparrow\rangle \rightarrow |P_{3/2}, m_J = 3/2\rangle$) by $\Delta_R \simeq -63.8$ GHz. This gives detunings of 15.6 GHz and 26.1 GHz respectively from the $|\uparrow\rangle \rightarrow |P_{3/2}, m_J = 1/2\rangle$ and $|\downarrow\rangle \rightarrow |P_{3/2}, m_J = -1/2\rangle$ transitions. Laser beam waists were $w_z \simeq 100 \mu\text{m}$ in the vertical (z -direction) and $w_x \simeq 1$ mm in the horizontal direction. Here we define the waist as the distance from the center of the beam over which the electric field intensity decreases by $1/e^2$ (i.e. $I(z) \sim e^{-(z/w_z)^2}$). With the small 2.4° incident angle each beam makes with respect to the plane of the crystal, this provided greater than 90% uniform electric field intensity across ion crystal arrays with $N < 250$.

We used linearly polarized laser beams. Let

$$\begin{aligned}\vec{E}_U(\vec{r}, t) &= \hat{\epsilon}_U E_U \cos(\vec{k}_U \cdot \vec{r} - \omega_U t) \\ \vec{E}_L(\vec{r}, t) &= \hat{\epsilon}_L E_L \cos(\vec{k}_L \cdot \vec{r} - \omega_L t)\end{aligned}$$

denote the electric fields of the upper and lower ODF beams. If ϕ_p is the angle of the laser beam electric-field polarization with respect to vertical polarization ($\hat{\epsilon} \cdot \hat{x} = 0$), then the AC Stark shift of the qubit states when illuminated by a single beam can be written

$$\begin{aligned}\Delta_{\uparrow, acss} &= A_\uparrow \cos^2(\phi_p) + B_\uparrow \sin^2(\phi_p) \\ \Delta_{\downarrow, acss} &= A_\downarrow \cos^2(\phi_p) + B_\downarrow \sin^2(\phi_p)\end{aligned}$$

where $A_\uparrow(A_\downarrow)$ is the Stark shift of the $|\uparrow\rangle(|\downarrow\rangle)$ state for a π -polarized beam ($\hat{\epsilon}$ parallel to the \hat{z} -axis) and $B_\uparrow(B_\downarrow)$ is the Stark shift of the $|\uparrow\rangle(|\downarrow\rangle)$ state for a σ -polarized beam ($\hat{\epsilon}$ perpendicular to the \hat{z} -axis). (Here we neglect the small σ polarization ($\propto \sin(2.4^\circ)$) that exists when $\phi_p = 0$.) The Stark shift of the qubit transition is

$$\Delta_{acss} = (A_\uparrow - A_\downarrow) \cos^2(\phi_p) + (B_\uparrow - B_\downarrow) \sin^2(\phi_p). \quad (5)$$

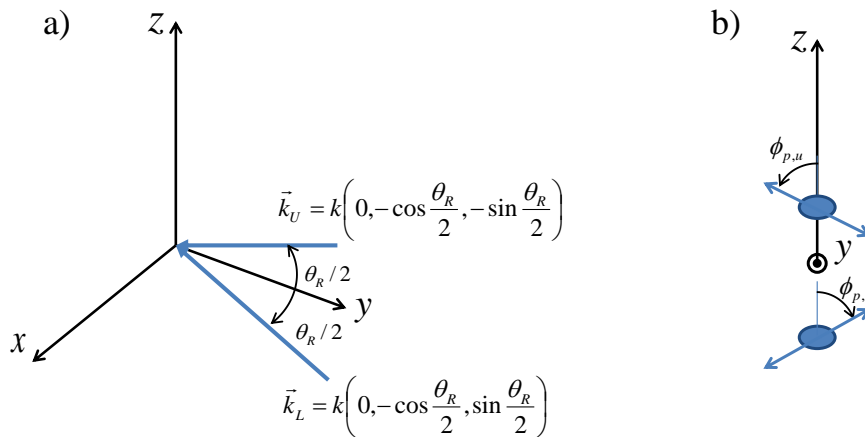


FIG. 4: Sketch of ODF laser beam setup. a) The ODF laser beams lie in the y - z plane at angles $\pm\theta_R/2$ with respect to the y -axis. b) View looking in the $-\hat{y}$ direction. The beams are linearly polarized but with different polarization angles relative to vertical polarization.

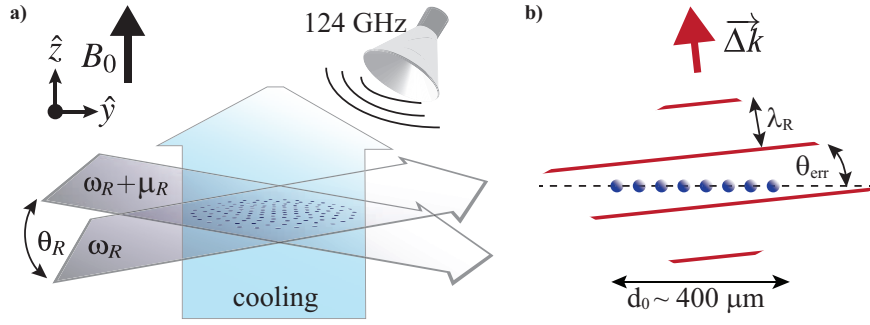


FIG. 5: Sketch of the 1D optical lattice wave fronts (red lines) generated by the ODF laser beams. These wave fronts need to be aligned with the ion planar array (represented by the blue dots). Here $\lambda_R = 2\pi/|\vec{\Delta k}| \approx 3.7 \mu\text{m}$ and θ_{err} denotes the angle of misalignment. $d_0 \sim 400 \mu\text{m}$ is the typical array diameter for $N \sim 200$ ions. With the wave front alignment technique discussed in the text we obtain $\theta_{\text{err}} < 0.05^\circ$.

If $A_\uparrow - A_\downarrow$ and $B_\uparrow - B_\downarrow$ have opposite signs, there is an angle which makes $\Delta_{\text{acss}} = 0$. For a laser detuning of $\Delta_R = -63.8 \text{ GHz}$, $\Delta_{\text{acss}} = 0$ at $\phi_p \simeq \pm 65^\circ$.

With $\Delta_{\text{acss}} = 0$ for each ODF laser beam, we exploit the freedom to choose their polarization in order to obtain a state-dependent force. Specifically we choose \vec{E}_U to have a polarization given by $\phi_{p,u} = 65^\circ$ and \vec{E}_L to have a polarization given by $\phi_{p,l} = -65^\circ$. In this case the interference term in the expression for the electric field intensity $(\vec{E}_U + \vec{E}_L)^2$ produces a polarization gradient which results in spatially dependent AC Stark shifts

$$\begin{pmatrix} A_\uparrow \cos^2(\phi_p) - B_\uparrow \sin^2(\phi_p) \\ A_\downarrow \cos^2(\phi_p) - B_\downarrow \sin^2(\phi_p) \end{pmatrix} 2 \sin(\delta k \cdot z + \mu_R t)$$

for the qubit levels. Here $\delta k \equiv |\vec{k}_U - \vec{k}_L| = 2k \sin(\frac{\theta_R}{2})$ is the wave vector difference between the two ODF laser beams, $\mu_R = \omega_U - \omega_L$ is the ODF beat note, and $\phi_p = |\phi_{p,u}| = |\phi_{p,l}|$. The spatially dependent AC Stark shift produces a state-dependent force $F_{\uparrow,\downarrow}(z, t) = F_{\uparrow,\downarrow} \cos(\delta k \cdot z - \mu_R t)$ where

$$\begin{pmatrix} F_\uparrow \\ F_\downarrow \end{pmatrix} = 2 \delta k \begin{pmatrix} A_\uparrow \cos^2(\phi_p) - B_\uparrow \sin^2(\phi_p) \\ A_\downarrow \cos^2(\phi_p) - B_\downarrow \sin^2(\phi_p) \end{pmatrix}.$$

In general $F_\uparrow \neq -F_\downarrow$. We operate at $\Delta_R = -63.8 \text{ GHz}$ where for $\Delta_{\text{acss}} = 0$ we also obtain $F_\uparrow = -F_\downarrow \equiv F$.

For a given $\phi_{p,u}$, $\phi_{p,l}$, and Δ_R we use straight forward atomic physics along with well known values for the energy levels and matrix elements of $^9\text{Be}^+$ to calculate F as a function of the electric field intensity $I_R = \frac{c\epsilon_0}{2} |E_L|^2 = \frac{c\epsilon_0}{2} |E_U|^2$ at the center of the laser beams. For $\theta_R = 4.8^\circ$ and $I_R = 1 \text{ W/cm}^2$, $F = 1.5 \times 10^{-23} \text{ N}$.

Wave Front Alignment

The ODF laser beams produce a 1D optical lattice characterized by the effective wave vector $\delta \vec{k}$ and beat note μ_R . In the previous section we assumed that $\delta \vec{k} \parallel \hat{z}$, or equivalently that the wave fronts of the lattice were aligned perpendicular to the \hat{z} -axis (magnetic field axis). If the wave fronts are not normal to the \hat{z} -axis as sketched in Fig. 5, then the time dependence of the optical dipole force seen by an ion in the rotating frame depends on the (x, y) position of the ion. This complicates the interaction generated by the optical dipole force and is avoided by careful alignment.

We used top-view images (images of the ion resonance fluorescence scattered along the magnetic field) from a single plane to measure a misalignment of the ODF wave fronts. For this measurement we set $\mu_R = 0$ (stationary 1D lattice) and detune the frequency of the ODF laser beams approximately 0.5 GHz below the $|\uparrow\rangle \rightarrow |^2P_{3/2} m_J = +3/2\rangle$ Doppler cooling transition. This small detuning generates sufficiently large AC Stark shifts on the cooling transition to measurably change the ion scatter rate from the Doppler cooling laser. With the Doppler cooling laser on and the ODF beams turned off we observe a spatially uniform, time-averaged image of a rotating planar crystal. With the ODF beams on, ions located in regions of high electric field intensity at the anti-nodes of the optical lattice are Stark shifted out of resonance with the Doppler cooling laser. This is what produced the dark bands in the top-view image

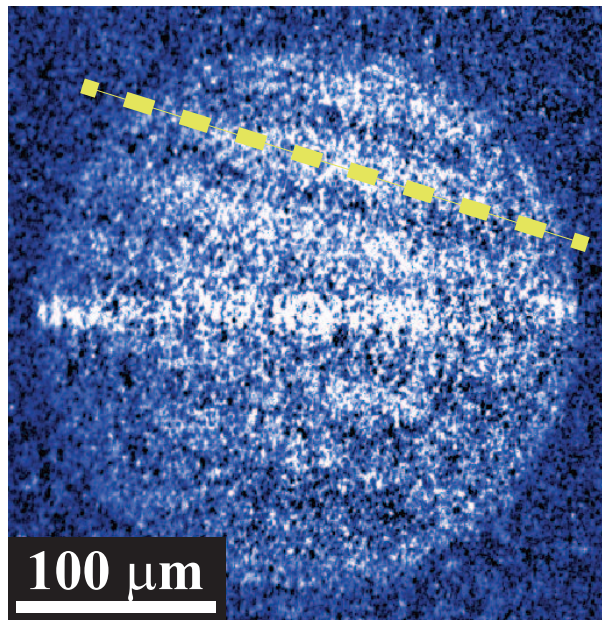


FIG. 6: Top-view image of the spatially inhomogeneous fluorescence from a single ion plane produced by the AC Stark from a static ($\mu_R = 0$) optical dipole force lattice with misaligned wave fronts. Dark bands are regions of high standing wave electric field intensity (parallel to the dashed yellow line). The bright horizontal feature bisecting the center of the image is fluorescence from the weak Doppler laser cooling beam directed perpendicular to the magnetic field. The image was obtained by subtracting a background image with the ODF beams off.

shown in Fig. 6. From images like this we determine how to move the ODF beams to align the wave fronts normal to \hat{z} . Improved alignment is indicated by a longer wavelength fringe pattern. With this technique we have aligned the ODF wave fronts with the planar array to better than $\theta_{err} \lesssim 0.05^\circ$.

Images like that shown in Fig. 6 were typically obtained with 1 s integration. This means the imprint of the 1D lattice on the planar arrays was stable during the integration time and indicates a phase stability of our 1D lattice of better than 1s. We note that direct fluorescence imaging of the 1D lattice, for example by tuning the ODF laser resonant with the Doppler cooling transition, is not viable. Even at low powers, resonantly scattered photons across the large horizontal waist of the ODF beams apply a large torque, causing the rotation frequency and radius of the array to rapidly change, typically driving the ions into very large radial orbits.

Spin-Motion Entanglement Produced by the Spin-Dependent Optical Dipole Force

With the wave vector $\delta\vec{k}$ of the 1D optical lattice aligned parallel to \hat{z} , the optical dipole force generated by the lattice is independent of the ion position and can be written

$$F_{\uparrow}(t) = -F_{\downarrow}(t) \equiv F \cos(\mu_R t) \quad (6)$$

where μ_R is the frequency difference between the ODF laser beams. More generally we allow for the possibility that the ODF laser intensity could be different for each ion, resulting in a different spin-dependent force F_j for each ion j ,

$$F_{j\uparrow}(t) = -F_{j\downarrow}(t) \equiv F_j \cos(\mu_R t) . \quad (7)$$

In the experimental set-up, the variation in F_j is less than 20%. The ODF interaction with the ion spins can be written as

$$H_{ODF} = - \sum_{j=1}^N F_j \cos(\mu_R t) \hat{z}_j \hat{\sigma}_j^z . \quad (8)$$

Here \hat{z}_j is the axial position operator for the j^{th} ion, which can be written in terms of the axial normal modes (\vec{b}_m, ω_m) of the planar array,

$$\hat{z}_j = \sum_{m=1}^N b_{jm} \sqrt{\frac{\hbar}{2M\omega_m}} (\hat{a}_m e^{-i\omega_m t} + \hat{a}_m^\dagger e^{i\omega_m t}) . \quad (9)$$

The eigenvectors are normalized so that $\sum_m |b_{jm}|^2 = \sum_j |b_{jm}|^2 = 1$. Both the eigenvectors \vec{b}_m and eigenfrequencies ω_m are calculated by solving for the ion equilibrium positions and diagonalizing the stiffness matrix obtained by Taylor expansion of the potential about the ion equilibrium positions [1].

The Hamiltonian H_{ODF} of Eq. (8) is time dependent. The evolution operator for H_{ODF} is obtained from a second order expansion of the Magnus formula [2, 3]

$$\hat{U}_{ODF}(t) = \exp \left[\frac{-i}{\hbar} \int_0^t H_{ODF}(t') dt' - \frac{1}{2\hbar^2} \int_0^t dt_2 \int_0^{t_2} [H_{ODF}(t_2), H_{ODF}(t_1)] dt_1 \right] . \quad (10)$$

Higher order terms do not contribute as the commutator $[H_{ODF}(t_2), H_{ODF}(t_1)]$ commutes with $H_{ODF}(t')$. Following the discussion of Ref. [3], $U_{ODF}(t)$ can be written

$$\begin{aligned} \hat{U}_{ODF}(t) &= \exp \left[\sum_j \left(\sum_m (\alpha_{jm}(t) \hat{a}_m^\dagger - \alpha_{jm}^*(t) \hat{a}_m) \hat{\sigma}_j^z \right) + i \sum_{j,k} J_{j,k}(t) \hat{\sigma}_j^z \hat{\sigma}_k^z \right] \\ &= \exp \left[\sum_j \left(\sum_m (\alpha_{jm}(t) \hat{a}_m^\dagger - \alpha_{jm}^*(t) \hat{a}_m) \hat{\sigma}_j^z \right) \right] \cdot \exp \left[i \sum_{j,k} J_{j,k}(t) \hat{\sigma}_j^z \hat{\sigma}_k^z \right] . \\ &\equiv \hat{U}_{SM}(t) \cdot \hat{U}_{SS}(t) \end{aligned} \quad (11)$$

The first term $U_{SM}(t)$ describes spin-dependent displacements $\alpha_{jm}(t)$ of the normal modes m where, for the $\cos(\mu_R t)$ time dependence of the interaction in Eq. (8),

$$\alpha_{jm}(t) = \frac{F_j b_{jm} z_{0m}}{\hbar (\mu_R^2 - \omega_m^2)} \left[\omega_m - e^{i\omega_m t} (\omega_m \cos(\mu_R t) - i\mu_R \sin(\mu_R t)) \right] . \quad (12)$$

Here $z_{0m} = \sqrt{\hbar/(2M\omega_m)}$. The second term $\hat{U}_{SS}(t)$ describes an effective spin-spin interaction where the pairwise coupling $J_{j,k}(t)$ is given by

$$J_{j,k}(t) = \frac{F_j F_k}{2\hbar^2} \sum_m \frac{b_{jm} b_{km} z_{0m}^2}{\mu_R^2 - \omega_m^2} \left\{ \frac{\omega_m \sin(\mu_R - \omega_m)t}{\mu_R - \omega_m} + \frac{\omega_m \sin(\mu_R + \omega_m)t}{\mu_R + \omega_m} - \frac{\omega_m \sin(2\mu_R t)}{2\mu_R} - \omega_m t \right\} . \quad (13)$$

For now we assume $\hat{U}_{SS}(t)$ can be neglected. We will discuss the validity of this assumption at the end of this section.

The interaction $\hat{U}_{SM}(t) = \exp \left[\sum_j \left(\sum_m (\alpha_{jm}(t) \hat{a}_m^\dagger - \alpha_{jm}^*(t) \hat{a}_m) \hat{\sigma}_j^z \right) \right]$ generates spin-motion entanglement that is the subject of this study. The commutator

$$\begin{aligned} [\alpha_{jm}(t) \hat{a}_m^\dagger - \alpha_{jm}^*(t) \hat{a}_m, \alpha_{km}(t) \hat{a}_m^\dagger - \alpha_{km}^*(t) \hat{a}_m] &= \alpha_{jm}(t) \alpha_{km}^*(t) - \alpha_{jm}^*(t) \alpha_{km}(t) \\ &= 0 \end{aligned}$$

because $\alpha_{jm}(t) \alpha_{km}^*(t)$ is real. Therefore we can write $\hat{U}_{SM}(t)$ as a product of individual spin displacements

$$\hat{U}_{SM}(t) = \prod_{j,m} \exp \left((\alpha_{jm}(t) \hat{a}_m^\dagger - \alpha_{jm}^*(t) \hat{a}_m) \hat{\sigma}_j^z \right) , \quad (14)$$

which is Eq. (4) of the Letter. By neglecting the spin-spin entanglement ($\hat{U}_{SS}(t)$) we can independently calculate the evolution of each spin j .

We now calculate the spin motion entanglement generated by $\hat{U}_{SM}(t)$ during the free precession period of a Ramsey sequence shown in Fig. 7(a). The calculation for the spin-echo sequence of Fig. 7(b) used in the experiments is identical except for a more complicated expression for the $\alpha_{jm}(t)$'s (see next section). Each spin j is prepared in state $|\uparrow\rangle$ at the start of the sequence. If an ODF is not applied during the free precession period, the spin is rotated to the dark $|\downarrow\rangle$ state by the final $\pi/2$ pulse of the sequence. With the application of a spin-dependent ODF, in general the spin is entangled with the motion at the end of the Ramsey sequence. We detect this spin-motion entanglement by measuring the probability of finding spin j in the $|\uparrow\rangle$ state. Let

$$\hat{U}_{SM}^{(j)}(t) = \exp \left(\sum_m (\alpha_{jm}(t) \hat{a}_m^\dagger - \alpha_{jm}^*(t) \hat{a}_m) \hat{\sigma}_j^z \right)$$

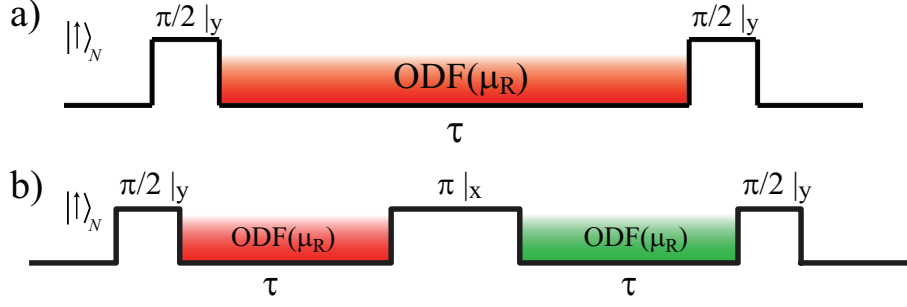


FIG. 7: Pulse sequences described in this supplemental material. a) Ramsey pulse sequence consisting of two $\pi/2$ rotations with an intermediate arm of duration τ during which the ODF is applied. b) The spin echo sequence repeated from Fig. 2(a) of the Letter which consists of two arms of duration τ .

denote the evolution of spin j by the spin-dependent ODF. By re-writing

$$\hat{U}_{SM}^{(j)}(t) = \cosh \left(\sum_m (\alpha_{jm} \hat{a}_m^\dagger - \alpha_{jm}^* \hat{a}_m) \right) + \sinh \left(\sum_m (\alpha_{jm} \hat{a}_m^\dagger - \alpha_{jm}^* \hat{a}_m) \right) \hat{\sigma}_j^z$$

we calculate

$$P_{\uparrow, SM}^{(j)} = \left\langle \left(\sinh \left(\sum_m (\alpha_{jm} \hat{a}_m^\dagger - \alpha_{jm}^* \hat{a}_m) \right) \right)^\dagger \sinh \left(\sum_m (\alpha_{jm} \hat{a}_m^\dagger - \alpha_{jm}^* \hat{a}_m) \right) \right\rangle_{th} \quad (15)$$

where $P_{\uparrow, SM}^{(j)}$ denotes the probability of measuring the $|\uparrow\rangle$ state for spin j produced by the $\hat{U}_{SM}(t)$ interaction, and $\langle \cdot \rangle_{th}$ denotes an expectation value averaged over a thermal (Maxwell-Boltzmann) distribution of modes. We evaluate Eq. (15) by writing the sinh functions in exponential form. It is then necessary to evaluate expressions of the form $\langle e^{\hat{A}} e^{\hat{B}} \rangle_{th}$ where \hat{A} and \hat{B} are operators which are linear in the raising and lowering operators \hat{a}_m^\dagger and \hat{a}_m . In this case we can make use of the result [4]

$$\langle e^{\hat{A}} e^{\hat{B}} \rangle_{th} = e^{(1/2) \langle \hat{A}^2 + 2\hat{A}\hat{B} + \hat{B}^2 \rangle_{th}}$$

to obtain

$$P_{\uparrow, SM}^{(j)} = \frac{1}{2} \left[1 - \exp \left(-2 \sum_m |\alpha_{jm}(t)|^2 (2\bar{n}_m + 1) \right) \right]. \quad (16)$$

Here $\bar{n}_m \simeq k_B T_m / (\hbar \omega_m)$ is the mean occupation number of a Maxwell-Boltzmann distribution characterized by temperature T_m . We measure the probability of detecting $|\uparrow\rangle$ averaged over all the ions $(\sum_j P_{\uparrow}^{(j)})/N$.

The simple result of Eq. (16) was obtained under the assumption that we could neglect $\hat{U}_{SS}(t)$ in Eq. (11). In general $\hat{U}_{SS}(t)$ will contribute to the measured $P_{\uparrow}^{(j)}$. This can be straight forwardly estimated when μ_R is tuned close to the COM mode ω_1 . In this case the resulting pair-wise interaction coefficients are identical for all ion pairs $J_{j,k}(t) \simeq J(t)$ with

$$J(t) = \frac{F^2}{2\hbar^2} \cdot \frac{z_{01}^2}{N(\mu_R^2 - \omega_1^2)} \left\{ \frac{\omega_1 \sin(\mu_R - \omega_1)t}{\mu_R - \omega_1} + \frac{\omega_1 \sin(\mu_R + \omega_1)t}{\mu_R + \omega_1} - \frac{\omega_1 \sin(2\mu_R t)}{2\mu_R} - \omega_1 t \right\}.$$

For small detunings $|\mu_R - \omega_1| \ll \omega_1$, $J(t)$ is approximately bounded by $|J(t)| \lesssim J \cdot t$ where

$$J = \frac{F^2}{2\hbar^2} \cdot \frac{z_{01}^2}{N(\mu_R^2 - \omega_1^2)} \omega_1.$$

The fully connected, uniform Ising interaction $\exp \left[iJ \left(\sum_{j,k} z_j^z z_k^z \right) t \right]$ obtained by coupling through the COM mode is identical to the single-axis twisting interaction analyzed by Kitagawa and Ueda [5]. We use the expressions given

in Ref. [5] to calculate $P_{\uparrow,SS}^{(j)}$, the probability of measuring spin j in the $|\uparrow\rangle$ state at the end of the Ramsey sequence due to the $\hat{U}_{SS}(t)$ interaction,

$$P_{\uparrow,SS}^{(j)} \simeq \frac{1}{2} [N8(Jt)^2] . \quad (17)$$

This expression is valid for short times t where $P_{\uparrow,SS}^{(j)}$ is small.

We obtain strong spin-motion entanglement for small detunings $|\mu_R - \omega_1| \ll \omega_1$. The magnitude of the coherently driven amplitude $\alpha_{j,m=1}(t)$ in the expression for $\hat{U}_{SM}(t)$ (Eq. (14)) and $P_{\uparrow,SM}^{(j)}$ (Eq. (16)) is maximized for a detuning $|\mu - \omega_1| \simeq \pi/t$ where

$$|\alpha_{j,1}|_{max} = \left| \alpha_{j,1} \left(t \simeq \frac{\pi}{|\mu_R - \omega_1|} \right) \right| \simeq \frac{F z_{01}}{\hbar \sqrt{N} |\mu_R^2 - \omega_1^2|} 2\omega_1 .$$

The above expression neglects terms of order $(\mu_R - \omega_M)/\omega_M$. Inserting $|\alpha_{j,1}|_{max}$ into Eq. (16) and assuming the exponent is small gives

$$P_{\uparrow,SM}^{(j)} \simeq \frac{1}{2} \left[2 |\alpha_{j,1}|_{max}^2 (2\bar{n}_1 + 1) \right] . \quad (18)$$

We compare $P_{\uparrow,SS}^{(j)}$ (Eq. (17)) with $P_{\uparrow,SM}^{(j)}$ (Eq. (18)),

$$\frac{P_{\uparrow,SS}^{(j)}}{P_{\uparrow,SM}^{(j)}} \simeq \frac{N \cdot 8 (Jt)^2}{2 |\alpha_{j,1}|_{max}^2 (2\bar{n}_1 + 1)} \simeq \frac{F^2}{4\hbar^2} \cdot \frac{z_{01}^2}{2\bar{n}_1 + 1} t^2 . \quad (19)$$

For the work reported here $F \sim 10^{-23}$ N, $z_{01} = \sqrt{\hbar/(2M\omega_1)} \sim 30$ nm, and $\bar{n}_1 \sim 10$ (Doppler cooling limit). For a typical interaction time $t \lesssim 10^{-3}$ s we calculate $P_{\uparrow,SS}^{(j)}/P_{\uparrow,SM}^{(j)} \lesssim 0.1$. Therefore for small detunings satisfying $|\mu_R - \omega_1| \lesssim (2\pi)/t \ll \omega_1$ we expect the spin-motion entanglement signature generated by $\hat{U}_{SM}(t)$ to dominate contributions due to $\hat{U}_{SS}(t)$. We note that the spin-motion entanglement signature $\left(P_{\uparrow,SM}^{(j)} \right)$ decreases with temperature.

For ground state cooling it may not be possible to neglect $\hat{U}_{SS}(t)$.

We do not estimate $P_{\uparrow,SS}^{(j)}$ for μ_R tuned close to modes ω_M other than the COM mode ω_1 . Therefore we do not know if it is a good approximation to neglect $\hat{U}_{SS}(t)$ when resonantly coupling to non-COM modes. However, we experimentally observe that neglecting $\hat{U}_{SS}(t)$ gives a good description of our experimental measurements for μ_R tuned close to the tilt (ω_2 and ω_3) and the next lower frequency modes (ω_4 and ω_5).

Spin Echo Sequence with Decoherence

To calculate $\alpha_{jm}(t)$ for the full spin echo sequence used in the experiment (see Fig. 7(b)), we must account for the accumulated phase difference between the ODF drive and oscillating ion cloud over the first arm and intermediate microwave π -pulse of combined duration $(\tau + t_\pi)$. This requires derivation of $\alpha_{jm}(t)$ for an ODF interaction with an arbitrary phase offset, ϕ , given by the more general

$$H_{ODF}(\phi) = - \sum_{j=1}^N F_j \cos(\mu_R t + \phi) \hat{z}_j \hat{\sigma}_j^z, \quad (20)$$

where $\phi = (\tau + t_\pi)(\mu_R - \omega_m) = (\tau + t_\pi)\delta_m$. Following the previous derivation of $\alpha_{jm}(t)$ for $\phi = 0$ (Eq. (12)), we obtain

$$\alpha_{jm}(t, \phi) = \frac{F_j b_{jm} z_{0m}}{\hbar (\mu_R^2 - \omega_m^2)} \left[\omega_m \cos(\phi) - i\mu_R \sin(\phi) - e^{i\omega_m t} \{ \omega_m \cos(\mu_R t + \phi) - i\mu_R \sin(\mu_R t + \phi) \} \right] . \quad (21)$$

We will now define a new α_{jm}^{SE} that may be substituted for α_{jm} in Eq. (14) to calculate P_{\uparrow} for the full spin echo sequence exhibiting arm durations of τ :

$$\alpha_{jm}^{SE} = \alpha_{jm}(\tau, \phi = 0) - \alpha_{jm}(\tau, \phi), \quad (22)$$

where the above expression is given explicitly in Eq. (6) of the Letter.

To justify implementation of Eq. (22), it is useful to calculate P_{\uparrow} for a single spin undergoing both the Ramsey and spin echo sequences. To simplify notation, we define the displacement operator $\hat{D}(\alpha_{jm}) = \exp(\alpha_{jm}\hat{a}_m^{\dagger} - \alpha_{jm}^*\hat{a}_m)$ which is applied separately to $|\uparrow_j\rangle \otimes |\psi_m\rangle$ and $|\downarrow_j\rangle \otimes |\psi_m\rangle$, where $|\psi_m\rangle$ is an arbitrary motional state of mode m . Assuming the state is initialized to $|\uparrow_j\rangle \otimes |\psi_m\rangle$, we calculate the result of the Ramsey sequence, $P_{\uparrow}^{(j)\text{Ramsey}}$, to be

$$P_{\uparrow}^{(j)\text{Ramsey}} = \frac{1}{4}\langle\psi_m|\left\{\hat{D}^{\dagger}(\alpha_{jm}(\tau,\phi)) - \hat{D}^{\dagger}(-\alpha_{jm}(\tau,\phi))\right\}\{h.c.\}|\psi_m\rangle, \quad (23)$$

where $\{h.c.\}$ denotes the Hermitian conjugate of the first bracketed expression. Here the arbitrary phase ϕ has no physical significance since its value is common to all displacements, and we have once again made the assumption that $F_{j\uparrow} = -F_{j\downarrow}$. However, the spin echo result given by $P_{\uparrow}^{(j)\text{SE}}$ is

$$P_{\uparrow}^{(j)\text{SE}} = \frac{1}{4}\langle\psi_m|\left\{\hat{D}^{\dagger}(-\alpha_{jm}(\tau,\phi))\hat{D}^{\dagger}(\alpha_{jm}(\tau,0)) - \hat{D}^{\dagger}(\alpha_{jm}(\tau,\phi))\hat{D}^{\dagger}(-\alpha_{jm}(\tau,0))\right\}\{h.c.\}|\psi_m\rangle \quad (24)$$

$$= \frac{1}{4}\langle\psi_m|\left\{\hat{D}^{\dagger}(\alpha_{jm}^{\text{SE}}) - \hat{D}^{\dagger}(-\alpha_{jm}^{\text{SE}})\right\}\{h.c.\}|\psi_m\rangle. \quad (25)$$

We obtain Eq. (26) from Eq. (25) using the multiplicative properties of \hat{D} and neglecting overall phase factors that leave $P_{\uparrow}^{(j)\text{SE}}$ unchanged. Note that Eq. (26) is identical to Eq. (24) after an appropriate redefinition of α_{jm} .

Finally, the derivation of Eq. (16) neglected the effects of spontaneous emission from the ODF laser beams. Decoherence of the Bloch vector due to spontaneous emission from off-resonant light is well studied in our system [6]. The qubit levels are closed under spontaneous light scattering; that is, spontaneous light scattering does not optically pump an ion to a different ground state level outside of the two qubit levels. In the presence of off-resonant laser light, the decrease in the Bloch vector due to spontaneous scattering during the arms of a spin-echo sequence is

$$P_{\uparrow,\text{spont}}^{(j)} = \frac{1}{2} [1 - \exp(-\Gamma \cdot 2\tau)].$$

Here $\Gamma \equiv (\Gamma_{\text{Ram}} + \Gamma_{\text{el}})/2$ has contributions from both Raman scattering and elastic Rayleigh scattering that can be calculated from the laser beam parameters. With the spin echo sequence, we account for spontaneous emission by modifying Eq. (16) as follows

$$P_{\uparrow,SM}^{(j)\text{SE}} = \frac{1}{2} \left[1 - e^{-\Gamma 2\tau} \exp\left(-2 \sum_m |\alpha_{jm}^{\text{SE}}|^2 (2\bar{n}_m + 1)\right) \right],$$

where τ is the length of time of a single arm of the spin-echo sequence.

-
- [1] J. W. Britton et al., *Nature* **484**, 489 (2012).
 - [2] S.-L. Zhu and Z. D. Wang, *Phys. Rev. Lett.* **91**, 187902 (2003).
 - [3] K. Kim, M.-S. Chang, R. Islam, S. Korenblit, L.-M. Duan, and C. Monroe, *Phys. Rev. Lett.* **103**, 120502 (2009).
 - [4] N. W. Ashcroft and N. D. Mermin, *Solid State Physics* (Saunders College, Philadelphia, 1976).
 - [5] M. Kitagawa and M. Ueda, *Phys. Rev. A* **47**, 5138 (1993).
 - [6] H. Uys, M. J. Biercuk, A. VanDevender, C. Ospelkaus, D. Meiser, R. Ozeri, and J. J. Bollinger, *Phys. Rev. Lett.* **105**, 200401 (2010).